Constructing the Universe with Clusters of Galaxies, IAP 2000 meeting, Paris (France) July 2000
Florence Durret & Daniel Gerbal eds.

BIASES IN SPECTRAL FITS OF UNRESOLVED NON-ISOTHERMAL X-RAY CLUSTERS AND GROUPS OF GALAXIES

F. Magnard[1], G.A. Mamon[1,2], F. Durret[1,2], D. Gerbal[1,2]
[1] Institut d'Astrophysique de Paris (CNRS UPR 341), 98bis Bd Arago, F-75014 Paris, France
[2] DAEC, Observatoire de Paris (CNRS UMR 8631), F-92195 Meudon Cedex, France

Using simulated spectra, we estimate the biases in the parameters describing the intra-cluster plasma, as obtained from spectral fits of spatially unresolved, polytropic non-isothermal X-ray clusters and groups of galaxies for various spectro-imaging instruments on X-ray telescopes (with an emphasis on XMM-Newton). We find that for typical observational parameters, the temperature obtained from single-temperature fits is equal, within $\simeq 10\%$ to the emission-weighted temperature, but underestimated but up to 20% when a cooling flow is present (high temperature clusters). These results are little affected by the metal abundance of the plasma, the signal-to-noise ratio of the observations (above some minimum, rarely reached by ROSAT/PSPC or Asca) and the spectral resolution of the instrument. Estimations of metal abundances and hydrogen absorptions are little biased, excepted in presence of a cooling flow. The residual of single temperature fits tend to be largest near 1 keV and we suggest a χ^2 analysis on grouped energy channels in the range $0.7 - 1.3$ keV.

1 Aim

How does non-isothermality of the intracluster medium affect X-ray diagnostics of unresolved clusters.

To answer this question, we simulate multi-temperature spectra, using a restricted set of parameters, summing up the spectra of different shells. We convolve the final spectra with the telescope and instrument response functions, fit the plasma properties (temperature, metal abundance, absorbing Hydrogen column), and compare to the input parameters, and emission-weighted temperature.

2 Method

2.1 Synthetic spectra

We model the spectra using `XSPEC`, version 11.0. The plasma is simulated using the `MEKAL` model (1; 2), which includes thermal bremsstrahlung and over 5000 emission lines. We adopt metal abundances in the solar ratio, taken from (3), who suggest that Fe is 30% lower than the standard *photospheric* value quoted by (4). Photoelectric absorption by Hydrogen and Helium is taken from (5), assuming a standard galatic absorbing column of $\mathrm{N_H} = 3 \times 10^{20}$ cm^{-}2.

Table 1: Polytropic index γ as a function of β (β-model for the density) and α (power law temperature slope).

$\beta \setminus \alpha$	0	1/7	2/7
0.55	1	1.08	1.17
0.8	1	1.06	1.12

A synthetic spectrum $S(E)$ is built by integrating over volume the emission of a sphere of gas:

$$S(E) = \frac{1}{4\pi D(z)^2} \int_0^\infty \epsilon \left[E, T(r), Z, n_e(r)\right] \mathrm{d}V(r) ,$$

where $D(z)$ is the luminosity distance at redshift z, $T(r)$ the temperature profile, Z the metal abundance, $n_e(r)$ the electronic density profile and $\mathrm{d}V(r)$ is the differential volume of a sphere intersected with the observation cylinder of projected radius r_{cyl} (i.e. the field of view of the X-ray instrument):

$$\mathrm{d}V(r) = \begin{cases} 4\pi r^2 \mathrm{d}r & \text{if } r < r_{\mathrm{cyl}} \\ 4\pi r^2 \left[1 - \sqrt{1 - (r_{\mathrm{cyl}}/r)^2}\right] \mathrm{d}r & \text{otherwise} \end{cases}$$

The electron density profile is taken as a β model

$$n_e(r) = n_{e_0} \left[1 + \left(\frac{r}{r_c}\right)^2\right]^{-3\beta/2} ,$$

where r_c is the core radius of the gas distribution.

We assume a polytropic temperature profile:

$$T(r) \propto n_e(r)^{\gamma-1} = T_0 \left[1 + \left(\frac{r}{r_c}\right)^2\right]^{-\alpha/2} ,$$

which has an asymptotic slope $\alpha = -3\beta(\gamma - 1)$, so that $\gamma = 0$ leads to an isothermal profile.

The temperature profile is chosen either isothermal (as a reference, $\alpha = 0$), or with $\alpha = 2/7$, as predicted in models of imperfect electronic conduction (6) that match the projected temperature profile of (7), or with a midway slope 1/7. The correspondence between the polytropic index γ and our values of α and β is given in Table 1. Simulations with a cooling flow are also made, using the `XSPEC` model `mkcflow` convolved with its own hydrogen column absorption. Parameters of the model are : a lower temperature set to 0.01 keV, a hydrogen absorption of $6 \times 10^{20}\mathrm{cm}^{-2}$ (double the standard galactic value), a higher cooling flow temperature tied to the central temperature of the envelope, and a mass accretion rate following the law $\dot{M} = 35.5[L_X/(10^{44}\ \mathrm{h}^{-2}\,\mathrm{erg\,s}^{-1})]^{0.7}\mathrm{M}_\odot/\mathrm{yr}$, that is a visual fit to the $\dot{M} - L_{\mathrm{bol}}$ figure from (8).

Throughout this paper, we suppose the electronic density to be equal to the Hydrogen density ($n_e = n_H$) for simplicity. The total flux determined from fit parameters will then be overestimated by 8% because of He^{++}.

The emission function is evaluated by Gauss-Legendre integration on 40 shells of given temperature and density.

The synthetic spectra $S(E)$ are finally functions of T_0, r_c, β, α, redshift z, metal abundance Z. We assign standard cluster values gave to these parameters given in Table 1. We choose Abell 85 as our *reference* cluster. No relations between β and T, and between r_c and T were imposed, because although some theoretical relations may be derived between these parameters, they are not supported by observations (see 9 and 10). Normalization follows the $L_X - T$ relation from (11) for clusters and from (12) for groups (the cooling flow is not taken into account is this normalization). The exposure time is set to 30 ks, except for redshift $z = 1$, where it was increased to 100 ks.

A cut-off radius is set to the field of view of the instrument, i.e. $30'$ for XMM-Newton EPIC, $8.4'$ for Chandra ACIS BI, $22'$ for Asca SIS and $40'$ for ROSAT-PSPC.

We compare the fitted temperature with the emission-weighted temperature defined by :

$$T_{\mathrm{ew}} = \frac{\int \mathrm{d}E \int T \epsilon(E, T, Z, n_e)\,\mathrm{d}V}{\int \mathrm{d}E \int \epsilon(E, T, Z, n_e)\,\mathrm{d}V} \tag{1}$$

Figure 2 shows how T_{ew}/T_0 varies with α and β for the `XSPEC` MEKAL plasma model. For a given T_{ew}/T_0, β is roughly linear with α, i.e. T_{ew}/T_0 could be approximated with a form like $(\alpha - b)/\beta$.

Figure 1: Parameters of the simulated spectra.

β	0.55 and 0.8
r_c	300 kpc
α	0, 1/7, 2/7
redshift	0.05, 0.2, 1
metallicity ($Z_\odot$)	0.3, 0.1, 1
T_0 (keV)	0.5, 1, 2, 4, 8, 16

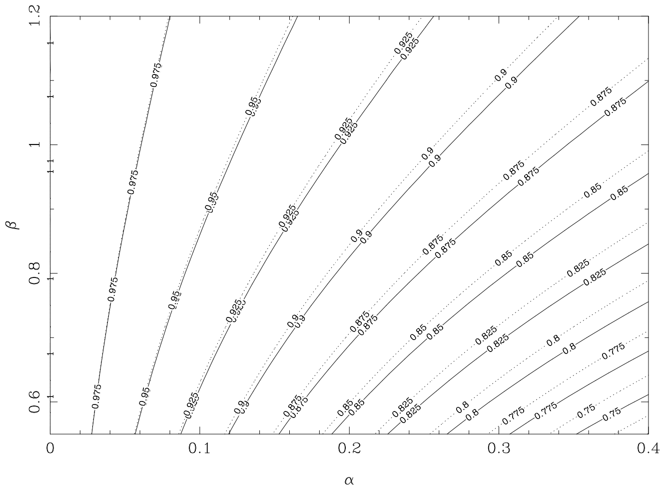

Figure 2: Theoretical iso-T_{ew}/T_0 curves for a MEKAL plasma model for different values of β and α. *Solid* and *dotted contours* represent $T = 5$ keV clusters and 1 keV groups, respectively (with metal abundance fixed at 30% solar).

2.2 Convolution with the telescope response function

The theoretical spectra are convolved with the telescope and instrument response functions using `XSPEC`. We used the available response matrix, valid at the center of the focal plane (`.rsp` files).

Our model spectra suppose that the cluster is centered on the detector. The energy resolution of the instrument is taken into account but not the spatial PSF.

After convolution, the spectrum is also binned, using `grppha` from FTOOLS softwares, to guarantee a minimum of 25 counts per bin.

2.3 Fitting

We treated the simulated spectra as if they were real data from effective observations, without any *a priori*, except the redshift. We used the `XSPEC` standard (modified Levenberg-Marquardt) minimization method for fitting.

The synthetic spectra are fitted with the following models:

- single temperature model (`XSPEC: model phabs(mekal)`)
- two temperature model (`XSPEC: model phabs(mekal+mekal)`)
- single temperature + cooling flow model (`XSPEC: model phabs(mekal)+phabs(mkcflow)`)

The significant free parameters are T, Z and N_H. We tried tied and free metal abundances in the two temperature models, but the later appeared to have too many parameters. Error bars are given by the fitting routine. They are underestimated by $\simeq 40\%$ relative to 90% errors given by a proper, but very time consuming, `XSPEC` error routine.

For the two-temperature models the initial guess was $T_h = T_0$ and $T_c = T_0/10$.

3 Results

We consider in this section results for XMM-Newton. Chandra gives similar results, ROSAT poor ones, and Asca intermediate ones.

3.1 Fitted versus emission-weighted temperature

Figure 3 shows the fitted temperatures in the idealized case of spectra with no Poisson noise. For isothermal simulations ($\alpha = 0$), the fitted parameters are found equal to the input ones, as they should be. For non-isothermal profiles, we find that $T_{\rm ew}$ is close to the fitted temperature $T_{\rm fit}$ to $\simeq 4\%$.

Figure 4 shows that, for realistic spectra with Poisson noise included, the fitted temperature $T_{\rm fit}$ is little biased (less than 10%) except for very cold clusters (groups) where $T_{\rm fit}$ can be 20% lower than $T_{\rm ew}$. But as these clusters have a weak emission, error bars are quite big.

Figure 5 shows that the two temperature fits with noise give higher and lower temperatures equally spaced from $T_{\rm ew}$, with higher offsets for steeper temperature profiles. But the lower temperature gas contributes to less than 1% of the total emission measure, except for cold and steep temperature profiles where it can reach 10% (the low temperature spectrum tunes the emission lines while the hot one drives the slope).

The presence of a cooling flow pulls the fitted temperature downward, depending on its proportion in the spectrum. For very hot clusters, where 50% of the emission in the field of view is due to their cooling flow, the fitted temperature can be $\simeq 20\%$ lower than the $T_{\rm ew}$.

When fitting with a single temperature + cooling flow model, the CF spectrum governs the low temperature part, leading to a better fit, even when no CF is present in the simulation. But a look at the residuals shows that it is not as good as the 2-temperature fit in this latter case.

3.2 Fit results on the metal abundance

Figure 6 indicates that the metallicity is well constrained (with XMM-Newton) except for very low temperatures where it is under evaluated for $T_{\rm fit} \simeq 1$ keV for steep temperature profiles. We can interpret this effect as due to the correlation between fitted temperature and metallicity for low temperature groups.

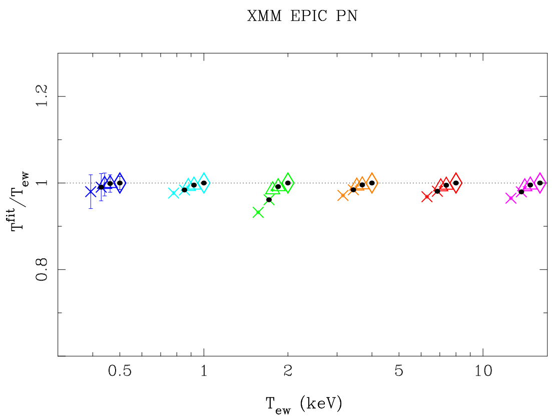

Figure 3: Ratio of fitted to emission-weighted temperature vs. emission weighted temperature for a single temperature fit, in the ideal case of clusters with no Poisson noise included. The spectra are simulated through the XMM-Newton EPIC detector. *Diamonds* are for $\alpha = 0$, *crosses* for $\alpha = 1/7$ and *triangles* for $\alpha = 2/7$. The *black dots* at the centers of symbols indicate $\beta = 0.8$, with $\beta = 0.55$ otherwise. Throughout this paper, the colors code the central temperature T_0 : blue for 0.5 keV, cyan for 1 keV, green for 2 keV, orange for 4 keV, red for 8 keV and magenta for 16 keV.

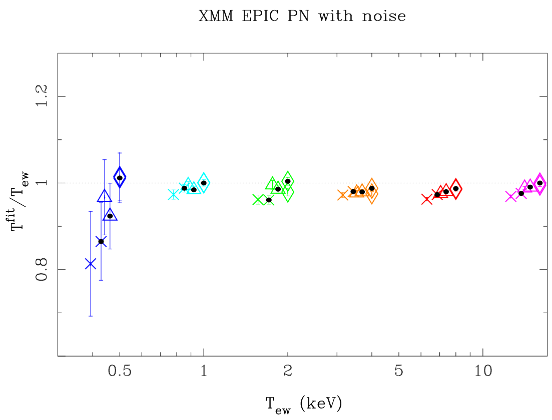

Figure 4: Same as Fig. 3 with Poisson noise included (30ks integration time of a simulated cluster at $z = 0.05$).

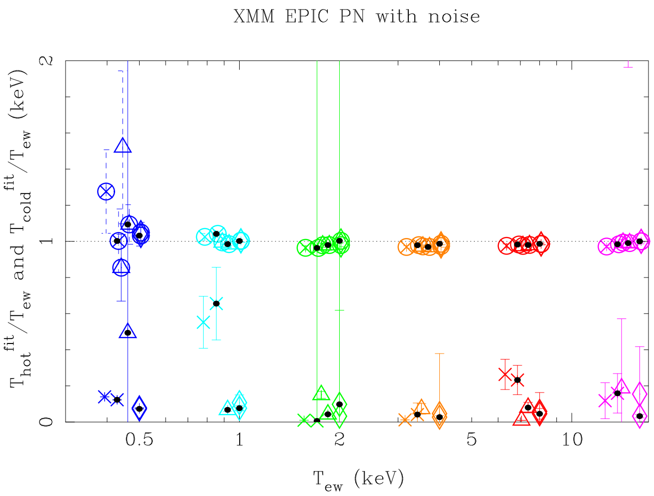

Figure 5: Same as Fig. 4 for two temperature fits. The *circles* around symbols refer to the component with the highest emission measure.

The temperature affects two main features of a `MEKAL` model: the slope (Bremsstrahlung emissivity) and the emission lines. The strongest lines in the fit are the Fe lines around 1 keV. They become more luminous as T is lowered and as Z is increased.

In figure 7, this bias is removed in a two temperature fit, where the metal abundances of the two components are tied.

As we choose, in our simulations, to give the same metal abundance to the cooling flow and to the IGM, the presence or not of the latter does not change this result.

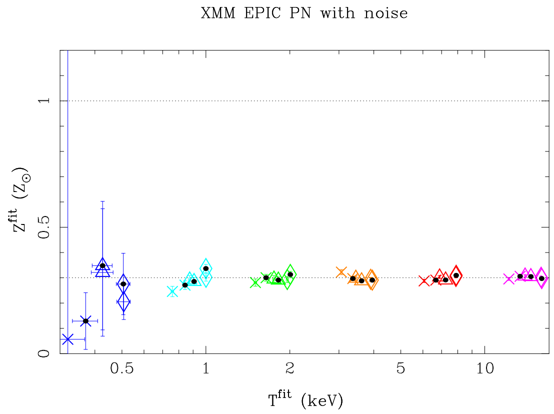

Figure 6: Fitted metallicity vs. fitted temperature in the single temperature model fit (XMM-Newton/EPIC 30 ks observation of $z = 0.05$ clusters, Poisson noise included). The input metal abundance ($Z = 0.3\,Z_\odot$) is shown as the *horizontal line*.

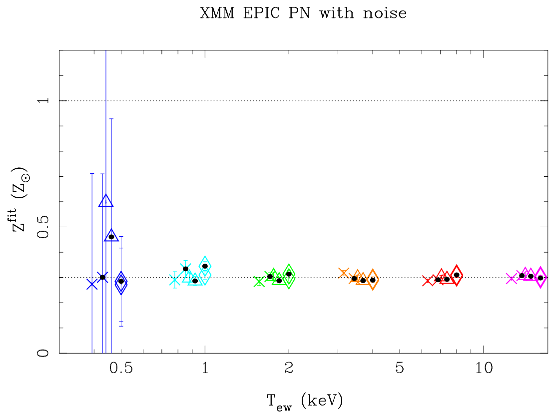

Figure 7: Same as Fig. 6, but for two-temperature fits (metal abundances tied).

3.3 Fit results on the absorbing Hydrogen column

Figure 8 shows that the fitted Hydrogen photo-electric absorption is well constrained for $T > 2$ keV, but the size of its error bars below this temperature led us to freeze this parameter for the coldest cases.

The presence of a cooling flow leads to an absorbing column that is underestimated by $\simeq 30\%$ (Fig. 9). N_H was frozen for low central temperatures (0.5 and 1 keV) because of its too strong influence on the resulting spectrum (very big error bars, bad estimation).

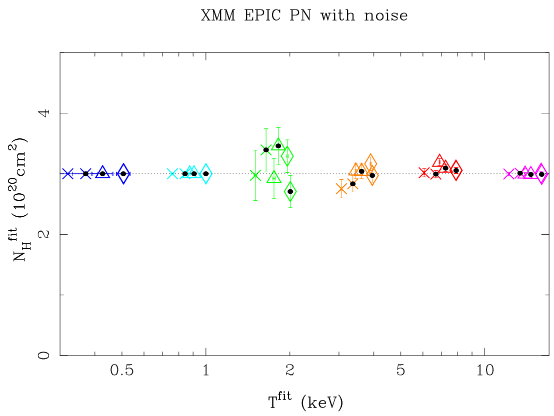

Figure 8: Fitted Hydrogen column N_H vs. fitted temperature in the single temperature fit (XMM-Newton/EPIC 30 ks observation of $z = 0.05$ clusters, Poisson noise included). The input Hydrogen column ($N_H = 3 \times 10^{20}$ cm^2) is shown as the *horizontal line*.

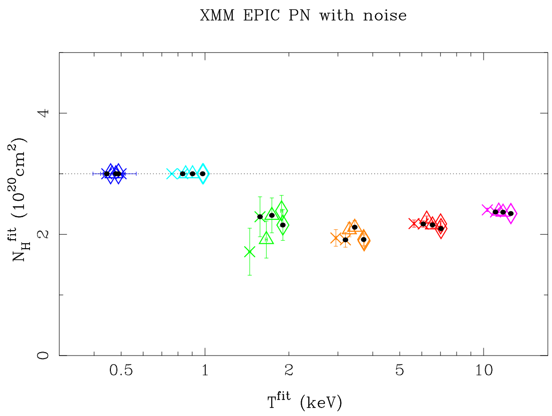

Figure 9: Same as Fig. 8 with a cooling flow.

3.4 Fit results on the mass deposition rate of cooling flows

The mass deposition rate of cooling flows ($\dot{M}$) is well constrained for hot nearby clusters ($z = 0.05$, Fig. 10), negligible compared to the overall emission when no CF is present, but $\dot{M}$ is very badly estimated at $z = 1$ (Fig. 11) where it reaches $10^4\,\mathrm{M}_\odot/\mathrm{yr}$ when no cooling flow were included in the simulation (Fig. 12)...

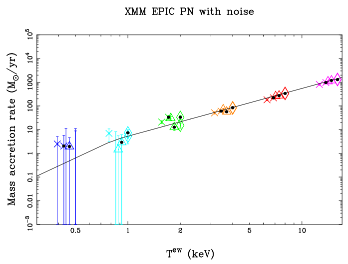

Figure 10: Fitted mass deposition rate vs. emission weighted temperature on a simulation IGM gas + CF (XMM-Newton/EPIC 30 ks observation of $z = 0.05$ clusters, Poisson noise included). The input values are shown by the solid line.

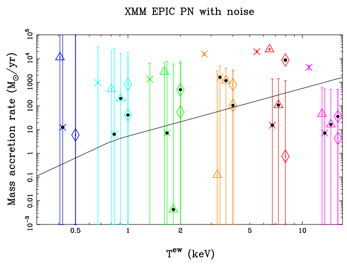

Figure 11: Same as Fig. 10 at $z = 1$ with 100 ks observation time.

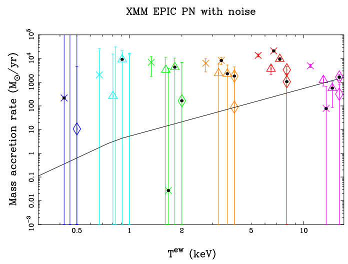

Figure 12: Same as Fig. 11 although no cooling flow model is present in the simulation.

3.5 Patterns in fit residuals

As illustrated in Figure 13, the single temperature fit without noise shows some patterns in the residuals for a set of parameters which strengthen the iron lines around 1 keV (giving a higher contribution to the cooler parts of the gas, i.e. low β, high α and low T_0). The residuals are most visible around 1 keV. The visible pattern is similar to the one in the residues of the single temperature fits of (13).

Figure 14 shows that this pattern remains visible between 0.7 and 1.3 keV when Poisson noise is included. Although the reduced χ^2 will be close to unity, even when computed within this restricted energy range, one can use more stringent statistics that will find a significant pattern in the residuals. For example, in regions of persistent residuals, the reduced χ^2 (equal to $\langle [D_i - M(E_i)]^2/D_i \rangle$, where D is the data, M the model, and E_i the energy channel) will be n times larger when the energy channels are grouped together n by n.

On the other hand, simulations with a central temperature higher than 5 keV are very well fitted by a single temperature model, even without the inclusion of Poisson noise.

Figure 15 displays the residuals in two temperature fits, for the idealized case of no Poisson noise. The differences between the simulated and fitted spectra are then no longer visible. When Poisson noise is included, a second temperature component does not improve the fit.

Finally, Figure 16 shows the residuals for a cluster seen with XMM-Newton at $z = 1$. No strong feature is visible, although the field of view covers a wider area of the cluster, reaching the colder outer parts of the cluster.

4 Discussion and Conclusions

Chandra and XMM-Newton are able to provide maps of temperature and metal abundance for nearby clusters. But such maps require significant counts, and thus cannot be obtained for more distant clusters. For distant clusters, spectral analysis on the full, spatially unresolved cluster remains the only method of analysis that can be applied.

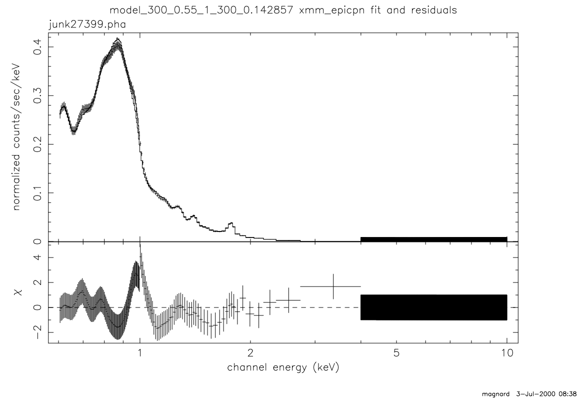

Figure 13: Single temperature **MEKAL** fit on a non-isothermal simulated MEKAL cluster (in the idealized case of no Poisson noise) seen through XMM-Newton. Parameters are $T_0 = 1\,\mathrm{keV}$, $\beta = 0.55$, $\alpha = 2/7$, $Z = 0.3 Z_\odot$, $N_H = 3 \times 10^{20}\mathrm{cm}^2$, $z = 0.05$. This single temperature fit cannot reproduce perfectly the features of this non-isothermal spectrum around 1 keV. Error bars reflect the uncertainties in the parameters for a 30 ks exposure time.

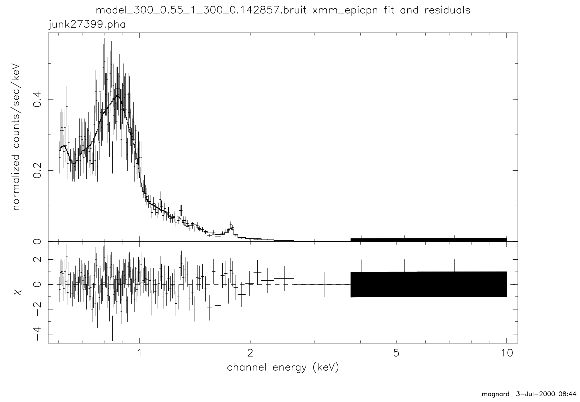

Figure 14: Same as Fig. 13, but with Poisson noise included, simulating an exposure time of 30 ks.

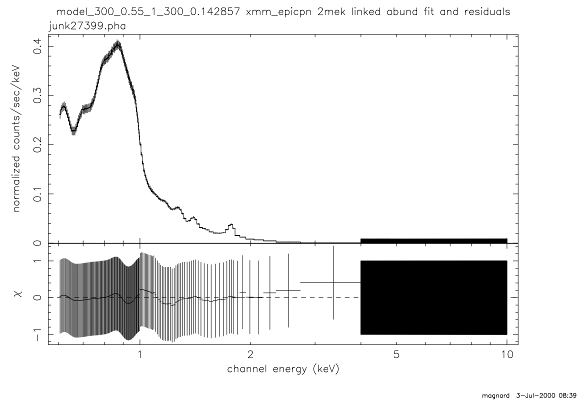

Figure 15: Same as Fig. 13, but for a two-temperature **MEKAL** fit (metal abundances tied).

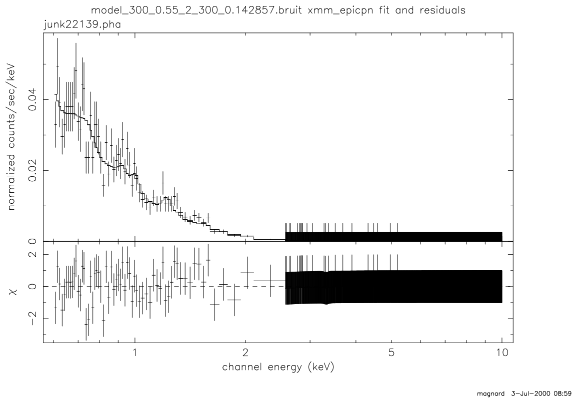

Figure 16: Same as Fig. 13, but for $T = 2\,\mathrm{keV}$, $z = 1$ and $t = 100\,\mathrm{ks}$.

If clusters are non isothermal, single temperature models will fit quite well the spectra (within large error bars due to the noise) but systematic biases remain:

- The fitted temperature is lower than the emission-weighted temperature for low temperature clusters and groups.
- The metal abundance is under-estimated for $T \simeq 1.5\,\mathrm{keV}$.

A non-isothermal spectrum (standard observation time of 30 ks) is very well fitted by a single temperature model. When Poisson noise is included, although residuals are not significant over the entire energy range, they are highly significant in the range $1 \pm 0.3\,\mathrm{keV}$ when energy channels are grouped together.

Our analysis does not strictly apply to the biases in the maps of temperature and metal abundance, because we restrict ourselves to centered observations, while the cells used in these maps are off-center. Nevertheless, we expect our results to provide useful guides for assessing the biases in these temperature and metallicity maps.

References

[1] R. Mewe, E. H. B. M. Gronenschild, and G. H. J. van den Oord. Calculated X-radiation from optically thin plasmas. V. A&AS, 62:197–254, 1985.

[2] R. Mewe, J. R. Lemen, and G. H. J. Van Den Oord. Calculated x-radiation from optically thin plasmas. VI - improved calculations for continuum emission and approximation formulae for nonrelativistic average Gaunt factors. A&AS, 65:511–536, 1986.

[3] U. Feldman. Elemental abundances in the upper solar atmosphere. Phys. Scr., 46:202–220, 1992.

[4] E. Anders and N. Grevesse. Abundances of the elements - meteoritic and solar. Geochim. Cosmochim. Acta, 53:197–214, January 1989.

[5] Monika Balucinska-Church and Dan McCammon. Photoelectric absorption cross sections with variable abundances. ApJ, 400:699, 1992.

[6] S. Dos Santos. Steady-state conduction-driven temperature profile in clusters fo galaxies. MNRAS, 2000. submitted.

[7] M. Markevitch, W. R. Forman, C. L. Sarazin, and A. Vikhlinin. The temperature structure of 30 nearby clusters observed with Asca: Similarity of temperature profiles. ApJ, 503:77–96, 1998.

[8] C. B. Peres, A. C. Fabian, A. C. Edge, S. W. Allen, R. M. Johnstone, and D. A. White. "A rosat study of the cores of clusters of galaxies - I. cooling flows in an X-ray flux-limited sample". MNRAS, 298:416–432, 1998.

[9] D. M. Neumann and M. Arnaud. Regularity in the X-ray surface brightness profiles of galaxy clusters and the M-T relation. A&A, 348:711–727, 1999.

[10] John S. Mulchaey and Ann I. Zabludoff. The properties of poor groups of galaxies. II. X-ray and optical comparisons. ApJ, 496:73, 1998.

[11] M. Arnaud and A. E. Evrard. The L_X – T relation and intracluster gas fractions of X-ray clusters. MNRAS, 305:631–640, 1999.

[12] S. F. Helsdon and T. J. Ponman. The intragroup medium in loose groups of galaxies. MNRAS, 315:356–370, 2000.

[13] D. A. Buote. X-ray evidence for multiphase hot gas with nearly solar Fe abundances in the brightest groups of galaxies. MNRAS, 311:176–200, 2000.